Materials Advances

ROYAL SOCIETY OF CHEMISTRY

PAPER

View Article Online
View Journal | View Issue

Cite this: *Mater. Adv.*, 2023, 4, 1146

Some interesting insights into the acetone sensing characteristics of monoclinic WO_3†

Puja Ghosh,[a] M. Manikandan,[bc] Shrabanee Sen *[a] and Parukuttyamma Sujatha Devi *[abc]

Considering the importance of tungsten oxide (WO_3) in fabricating acetone sensors for the non-invasive diagnosis of diabetes, it has become pertinent to understand the critical reasons behind the diverse and interesting acetone sensing behaviour of WO_3 nanomaterials. To find a solution for our quest to understand the effect of particle morphology and crystallographic modifications on the acetone sensing behaviour of WO_3, we have synthesized γ-monoclinic WO_3 nanoparticles by a hydrothermal technique and fibers by an electrospinning technique. The fabricated tubular-type sensor utilizing the synthesized WO_3 exhibited a distinct difference in the response towards different concentrations of acetone in the lower range, such as 10, 5, 2, 1, 0.8 and 0.5 parts per million (ppm). In contrast to the 84% sensing response of the WO_3 particle-based sensor towards 10 ppm acetone at an operating temperature of 200 °C, the fiber-based sensor exhibited a much better response of more than 90% at a lower operating temperature of 150 °C with improved recovery time. Based on various characterization techniques, it has been confirmed that both the synthesized materials exhibit an interesting crystallographic texture with preferred orientation along the 002 crystal facet, which is expected to chemisorb more oxygen molecules on the surface leading to the observed higher sensing performance at a lower temperature. Moreover, the excellent gas sensing performances of the WO_3 fiber-based sample could be attributed to the charge confinement and electron transfer ability of a one-dimensional (1D) structure with high surface-to-volume ratio, and the exposed highly reactive (002) plane with improved crystallinity which facilitates more chemisorbed oxygen molecules at a lower temperature (150 °C). We have also demonstrated the performance of the sensor at different humidity levels and acetone concentrations to prove its potential use in breath analysis. This study further envisages the potential of the WO_3-fibers for developing next-generation solid-state gas sensors for the non-invasive detection of diabetes.

Received 7th June 2022,
Accepted 20th December 2022

DOI: 10.1039/d2ma00651k

rsc.li/materials-advances

Introduction

Metal oxide (MO)-based gas sensors are operated by a change in conductance or resistance when the target gas atoms or molecules interact with the semiconductor surface, leading to conductometric or chemoresistive type gas sensing behaviour. In search of new oxides for next-generation gas sensing materials with higher response, lower operating temperature, and faster response-recovery time, tungsten oxide (WO_3) has been established as a promising material compared to other conventional materials to develop sensor devices for various flammable and toxic gases.[1,2] WO_3 has superior performance over other materials due to its excellent physical and chemical properties and unique crystallographic modifications. The WO_3-based gas sensors have been reported to be emerging as powerful sensors particularly for NO_2 and acetone sensing.[3–5] The sensing response of WO_3 towards volatile organic vapours like acetone has drawn renewed attention in developing sensors for breath analysis.[6,7]

WO_3 exists in five different crystallographic modifications at different temperatures such as a low-temperature monoclinic ε-WO_3, a triclinic WO_3, a room temperature monoclinic γ-WO_3, an orthorhombic WO_3 and a tetragonal WO_3 phase. Among these, the monoclinic phase has been reported to be thermodynamically the most stable phase. However, other metastable phases, particularly orthorhombic WO_3 (o-WO_3), also invited researchers' attention due to its unique hexagonal and trigonal tunnels, making it a promising gas sensing material.[8] Along with the crystallographic phase, morphology also plays a critical role in governing the sensing mechanism. Compared to

[a] *Functional Materials and Devices Division, CSIR-Central Glass and Ceramic Research Institute, Jadavpur, Kolkata 700032, India. E-mail: shrabanee@cgcri.res.in*
[b] *Chemical Sciences and Technology Division, CSIR-National Institute for Interdisciplinary Science and Technology, Thiruvananthapuram 695019, India. E-mail: psujathadevi@niist.res.in*
[c] *Academy of Scientific and Innovative Research (AcSIR), Ghaziabad 201002, India*

† Electronic supplementary information (ESI) available. See DOI: https://doi.org/10.1039/d2ma00651k

other structures, one-dimensional (1D) structures such as nanofibers, nanorods, nanowires, nanotubes, *etc.* are a promising choice due to their higher surface area and lower agglomeration tendency that can increase the electron flow and affect the reaction between surface adsorbed oxygen and gas molecules, which can improve the gas sensing properties.

Interestingly, there are many reports on the gas sensing behaviour of WO_3 in various forms for various gases as illustrated below. Li *et al.* reported ethanol sensing properties using hydrothermally synthesized WO_3 nanotube bundles.[9] Cai and coworkers reported a single crystalline WO_3 nanowire on an FTO substrate, which exhibited a sensing response towards 500 ppm NO at 300 °C.[10] WO_3 nanofibers using the electrospinning method with controlled particle distribution and enhanced porous structure have been explored for ammonia[11,12] and acetone sensing.[13] Han *et al.* reported better gas sensing performance of triclinic WO_3 with exposed (010) facets towards 1-butylamine.[14]

A biomarker is one of the most exciting tools to detect various diseases and monitor the health status and other abnormalities in health conditions and other disease states, prognoses and predictions.[15] It has been clinically found that the acetone concentration in the breath of human beings can be correlated with many diseases, such as diabetes, asthma, lung cancer, and halitosis. For a diabetic patient, the acetone concentration level has been found to be 1.7 to 3.7 parts per million (ppm)s in human breath; for pre-diabetic, the range is between 0.9–1.7 ppm, and for the normal condition the range lies within 0.3–0.9 ppm.[16,17] For this reason, modern breath analysis has concentrated on acetone as a biomarker for diabetes and developing chemiresistive metal oxide-based acetone sensors is the future of non-invasive point-of-care diabetes management. There are interesting reports on the acetone sensing performance of WO_3 polymorphs. S. Sun *et al.* in 2019 reported an integrated acetone monitoring system for low power consumption with graphene-tungsten oxide nanocomposites exhibiting higher sensitivity and fast response time.[18] Systems offering acetone detection for breath analysis with a Si-doped WO_3-based sensor material with increasing thermal stability and selectivity have also been reported for the application of diabetic detection.[19] A possible sensing mechanism towards the sensing of acetone vapour was proposed in 2013 by Yidong Zhang *et al.* using WO_3 microspheres synthesized *via* hydrothermal reaction.[20] Most of the reports on WO_3 sensors are based on monoclinic γ-WO_3 phases. However, there are also reports highlighting the selective detection of acetone by the unstable ε-WO_3 and faceted hexagonal phases.[21,22] In addition, there are also reports on the effect of various morphologies,[23,24] crystal orientations[25] and grain effects[26] on the acetone sensing characteristics of WO_3. The importance of this semiconducting material in fabricating acetone sensors for the non-invasive diagnosis of diabetes has thrown critical issues in understanding the actual reasons behind the diverse and interesting acetone sensing behaviour of WO_3 nanomaterials.

As reported by Jia *et al.*, WO_3 with (002) facets exhibited a higher acetone sensing response with better selectivity than exposed (100) facets.[27] Higher NO_2 sensing performance of WO_3 nanocolumn bundles with exposed (002) facets was also reported by J. J. Qi *et al.* for low temperature-based gas sensing.[28] The crystallographic orientation of the morphology, especially 1D, is another pivotal factor for fast, reliable, and low-level acetone gas detection. Considering the most stable and effective monoclinic phase, the (002) facet of WO_3 possesses the highest surface energy (1.56 J m^{-2}) compared with the (200) facet (1.43 J m^{-2}) and the (020) facet (1.54 J m^{-2}), and the (002) facet is more favourable for adsorbing reaction species to decrease the surface energy. The preferential orientation to the (002) plane of WO_3 is possibly more favourable in the absorption and redox of pollutants than the preferential orientation of (020) planes.[29]

In this work, a significant effort was devoted to understanding the combined effect of surface-active crystalline phase and morphology to address the acetone sensing characteristics of WO_3-based tubular sensors. To achieve a rapid, reliable, selective and low concentration detection of acetone at lower temperatures, we have synthesized WO_3 nanoparticles by a hydrothermal technique and WO_3 with a fiber-like morphology by an electrospinning technique and they were employed for acetone gas sensing at different concentrations and operating temperatures. Various physicochemical characterizations were coupled with electrical characterization to correlate the acetone gas sensing behaviour of the fabricated sensors. It was also envisaged to study the response of the sensors using both AC and DC measurements, which are complimentary techniques in understanding the sensing mechanism. It is noteworthy to mention here that WO_3 fibers are rarely reported as a low operating temperature acetone sensing material. The observed excellent sensing properties of the fabricated WO_3 fiber-based sensors are attributed to the nanoparticle interconnected fiber structure's porosity, which provides a much-enhanced surface area and abundant gas penetration pathways into the inner sensing layers for effective gas adsorption–desorption reactions and fast gas diffusion. Our major interest was to understand the above factors, which basically are important in fabricating acetone sensors that can differentiate various concentrations of acetone at lower temperature than the commonly reported 350 °C.[16–18]

Experimental section

Materials and methods

Materials. For particle synthesis, sodium tungstate dihydrate [$Na_2WO_4{\cdot}2H_2O$, 99.99%] and hydrochloric acid (HCl) [37%] from Merck, India were used. For fiber synthesis, polyvinylpyrrolidone [PVP, M_w = 55 000 mol g^{-1}] (99.99%) and ammonium metatungstate hydrate (AMT, 99.99%) were used from Sigma Aldrich and ethanol (99%) from Merck, India. All the chemicals were used as received without further purification.

Synthesis of WO_3 nanoparticles and nanofibers

WO_3 nanoparticles were prepared by adopting a hydrothermal process reported by Vemvasakis *et al.* (2015).[30] At first, 5 gm of sodium tungstate dehydrate ($Na_2WO_4{\cdot}2H_2O$) was dissolved in 150 ml deionized water to form a transparent solution.

Concentrated hydrochloric acid (37%) was added drop-wise to the solution to form a yellowish tungstic solution, which was transferred to a Teflon-lined autoclave for hydrothermal reaction at 95 °C for 24 h. The colored product formed during the hydrothermal process was centrifuged with deionized water several times. The washed precipitate was dried at 100 °C followed by calcination at 500 °C for 5 h.

For fabricating WO_3 nanofibers a modified process reported earlier by Wei *et al.* was employed.[31] A 27 wt% of polyvinylpolypyrrolidone (PVP) (M_W = 55 000) solution in 11.5 ml ethanol was added to 1.2 ml aqueous solution of 1.6 g ammonium metatungstate hydrate under stirring. The resulting solution was stirred for 4 h under ambient conditions to form a uniform viscous solution. For electrospinning, the viscous solution was transferred to a plastic syringe equipped with a metallic needle. The fibers were collected on a rotating drum collector placed at a 14 cm distance from the spinneret. The solution flow rate of 1 ml h^{-1} was controlled by a syringe pump, and a potential of 14 kV was applied between the spinneret and collector. The as-prepared fibers were calcined at 500 °C for 5 h at a heating rate of 2 °C min^{-1} to get the desired phase after the complete removal of PVP. The dried powder samples were collected for further use. The SUPER-ES-3 Electrospinning Unit (E-Spin Nanotechnology) was used for electrospinning synthesis.

Methods

The phase composition of the synthesized WO_3 samples was determined by the X-ray diffraction (XRD) method on an X'pert pro PAN analytical system with CuKα radiation (λ = 1.5406 Å). A Raman spectroscopic study was carried out to confirm the phase formation using a 514.5 nm Ar^+ green laser excitation source with 50 mW power on a STR500 Cornes Technologies system. Fourier transformed infrared (FTIR) spectra were acquired on a PerkinElmer, Spectrum two FTIR spectrometer. The X-ray photoelectron spectroscopy (XPS) measurements were carried out on a PHI 5000 Versa probe II scanning XPS microprobe (ULVAC-PHI, U.S.). The morphology of the WO_3 samples was determined using a field emission scanning electron microscope (FESEM) (LEO 430i, Carl Zeiss) and a transmission electron microscope (TEM) and a high-resolution TEM (HRTEM) operated at 300 kV (Tecnai G2 30ST, FEI). Furthermore, the specific surface area of the WO_3 samples was measured using a Quantachrome (iQ3) instrument after evacuation at 150 °C for 4 h. The direct current (DC) electrical measurements were performed using an Agilent multimeter (Model No. U1253A). Besides, alternating current (AC) measurements were carried out by a precision impedance analyzer (6500 B Wayne Kerr) within a wide frequency range from 100 Hz to 1 MHz.

WO_3-based sensor fabrication

To fabricate tubular sensing elements, the synthesized powder sample was ground smoothly in a motor pestle with isopropyl alcohol and coated uniformly on the surface of the alumina tube substrate having 3 mm length, 2 mm diameter and 0.5 mm thickness attached with Pt wire and gold-coated electrodes on both ends. For the heating of the sensors, a nichrome wire was used as a heating element inside the hollow substrate and the sensor was heated by using a DC voltage source (Keysight, E3630A). The substrates were well packed in customized sensor modules and exposed to different concentrations of gases (ChemixPvt. Ltd, Bangalore) inside the sensing chamber (~25 °C, % RH ~25%). Similar sensor fabrication details are also reported in our previous publications[32,33] The electrical resistance of the sensor device was measured by varying the operating temperature in the presence of air and acetone by using a digital multimeter (Agilent U1253A) with a constant voltage source (Keithley 228A) and the data was collected with the help of an Agilent GUI Data Logger. The sensitivity percentage (S%) was calculated as the function $\left[S(\%) = \frac{R_a - R_g}{R_a}\right]$ where R_a and R_g represent the electrical resistance of the sensor device in the presence of air and target gas acetone, respectively.

Results and discussion

Structural characterization of the synthesized WO_3 powder samples

To understand the structure and crystal phase of the powder samples after calcination at 500 °C, X-ray diffraction analysis was performed on the synthesized WO_3 particles (WP) and fibers (WF) as shown in Fig. 1(a). The XRD reflections of both WP and WF are sharp, which could be attributed to the high-

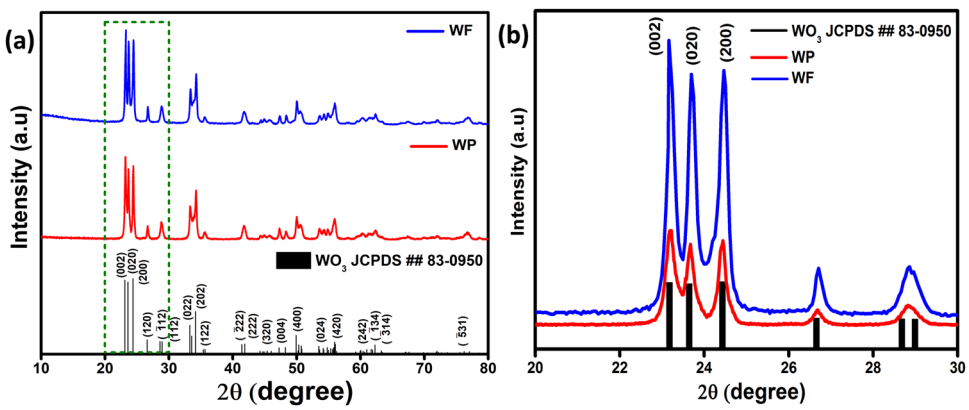

Fig. 1 (a) X-ray diffraction pattern of WP and WF samples and (b) magnified image of the highlighted area showing the preferred orientation of 002 reflections.

quality crystalline WO_3 phase formed during the annealing process (500 °C). All the diffraction peaks are indexed and well-matched with the JCPDS data card (No. 83-0950) of the monoclinic crystal structure of WO_3.

The lattice parameters calculated from the respective XRD patterns are a = 7.290 Å, b = 7.534 Å and c = 7.667 Å and β = 90.90° for the electrospun synthesized sample, and a = 7.299 Å, b = 7.524 Å and c = 7.673 Å and β = 90.898° for the hydrothermally synthesized sample. Furthermore, calcination at higher temperature assures the elimination of all the impurities and metastable oxides, leading to the stable monoclinic WO_3 phase. For further detailed analysis, the crystallite size (D) of the hydrothermally synthesized particles and electrospun WO_3 fibers was determined by using Debye Scherrer's formula as shown in eqn (i),

$$D = \frac{0.9\lambda}{\beta \cos\theta} \quad \text{(i)}$$

Here, λ is the X-ray wavelength, β is described as the full width at half maximum of the selected peak, and θ is the Bragg's angle.[34] The calculated crystallite size of the WO_3 particles and fibers was around 95 nm and 60 nm, respectively, implying that the fiber-like structure consists of a smaller crystallite size than the hydrothermally synthesized particles.

The three most intense reflections in the 2θ range of 22–26° could be indexed to the 002, 020 and 200 reflections of a monoclinic γ-WO_3 phase. It is also clear from the XRD patterns shown in Fig. 1(b) that the (002) reflections for both samples are significantly stronger than the standard pattern confirming a preferred orientation in the 002 direction.

Interestingly, on further comparison shown in Fig. 1(b), (002) reflections for both samples are significantly predominant compared to the other close facets. From eqn (ii), the relative texture coefficient of the crystal facet (TC_{002}) has been calculated.[35,36]

$$TC_{002} = \frac{I_{002}/I^0_{002}}{I_{002}/I^0_{002} + I_{200}/I^0_{002}} \quad \text{(ii)}$$

where I_{002} and I_{200} are the intensities of the (002) and (200) diffraction facets, respectively, and I^0_{002} and I^0_{200} are the corresponding intensities of the standard XRD patterns. Here, the relative texture coefficient of the (002) diffraction peak has been calculated over (200) for both fiber and particle samples. The calculated texture coefficient values are 0.552 and 0.521 for the WF and WP samples, respectively. It is clear from the magnified image of Fig. 1(b) in the range of 20° to 30° and the texture coefficient value calculated that the (002) plane is more exposed for the WO_3 fiber (WF) sample than particle (WP) and standard WO_3 indicating a preferred growth of the fibers in the (002) direction.

FTIR and Raman study of WO_3 particle and fiber samples

A Raman spectroscopic study was performed for the WP and WF samples, as shown in Fig. S1a (ESI†), which constitutes the W–O–W bending and stretching modes that appeared at ~272.43, 718.41 and 806.94 cm^{-1}, respectively, further confirming the successful formation of monoclinic WO_3. Raman bands appeared at <250 cm^{-1}, usually attributed to $(W_2O_2)_n$ chains and primarily assigned for bending vibration of W–O–W bonds. No additional distinct peaks were detected either at ~643 and 948 cm^{-1} for the hexagonal phase of WO_3 or ~759 and ~929 cm^{-1} due to the hydrous phase of WO_3, which indicates the successful formation of monoclinic WO_3.[37] The shoulder peak at ~615 cm^{-1} corresponds to the stretching vibration of O–W–O bonds originating from the monoclinic crystallographic orientation.[38] Moreover, the Raman band intensities of WF samples were escalated compared to WP samples. Furthermore, FTIR analysis was performed to understand the formation of the WO_3 structure and phase purity, as shown in Fig. S1b (ESI†). The broad peak that appeared at ~760 cm^{-1} is attributed to the W–O–W vibrational bond of the WO_6 octahedron in the crystal structure to form WO_3. The peak at ~815.17 cm^{-1} corresponds to the W–O–W stretching vibration bond. The peak at ~964 cm^{-1} is associated with the W═O stretching vibration, and the peak at ~1396 cm^{-1} is attributed to the bending vibration in W–OH.[39] Significantly, the absence of any peaks originating from PVP indicates complete removal during the preparation of the WF sample.

X-ray photoemission spectroscopic (XPS) analysis

The synthesized sample has been further analyzed by XPS study to investigate the chemical composition and oxidation state of the fundamental elements present in the synthesized samples. The survey spectrum of electrospinning and hydrothermally synthesized based samples is shown in Fig. 2(a). The characteristic peaks at 36 eV have been ascribed to W^{6+} with two binding energies of W $4f_{7/2}$ and W $4f_{5/2}$ as shown in Fig. 2(b) and the broad peak observed at 40.8 eV corresponds to W 5p. The XPS data confirms the presence of W with +6 oxidation state present in the synthesized samples.[40] The core level O1S spectra of WF and WP can be resolved into two Gaussian components as shown in Fig. 2(c) and (d) indicating the significant differences in oxygen states of the samples. The peaks centered at about 529.8 (O1) and 530.7 (O2) eV for the electrospun fibers and for the hydrothermally synthesized sample at about 529.2 (O1) and 530.6 (O2) eV. Here, the O1 component of the spectra is characteristic of O^{2-} ions and the O2 component is ascribed to the chemisorbed oxygen species at the grain boundaries. A higher amount of adsorbed oxygen ions are present in the WF samples, which could help in giving an enhanced adsorption of acetone on the surface resulting in a better performance.

Morphological analysis of the synthesized particle and fiber samples

Fig. 3(a), (b) and (d), (e) represent the field emission scanning electron microscopic (FESEM) images of WO_3 samples, having well developed granular particles and fiber morphologies, respectively. Single fibers having an overall length varying in the range of 1–2 μm and an average diameter of ~440 nm are clearly visible in Fig. 3(f). In comparison, the particles are more homogeneous with a granular disk-like structure with an average size of ~160 nm (Fig. 3(c)). The response of a sensor material strongly depends on the materials' surface area and crystallite size, and the sensitivity will be increased with

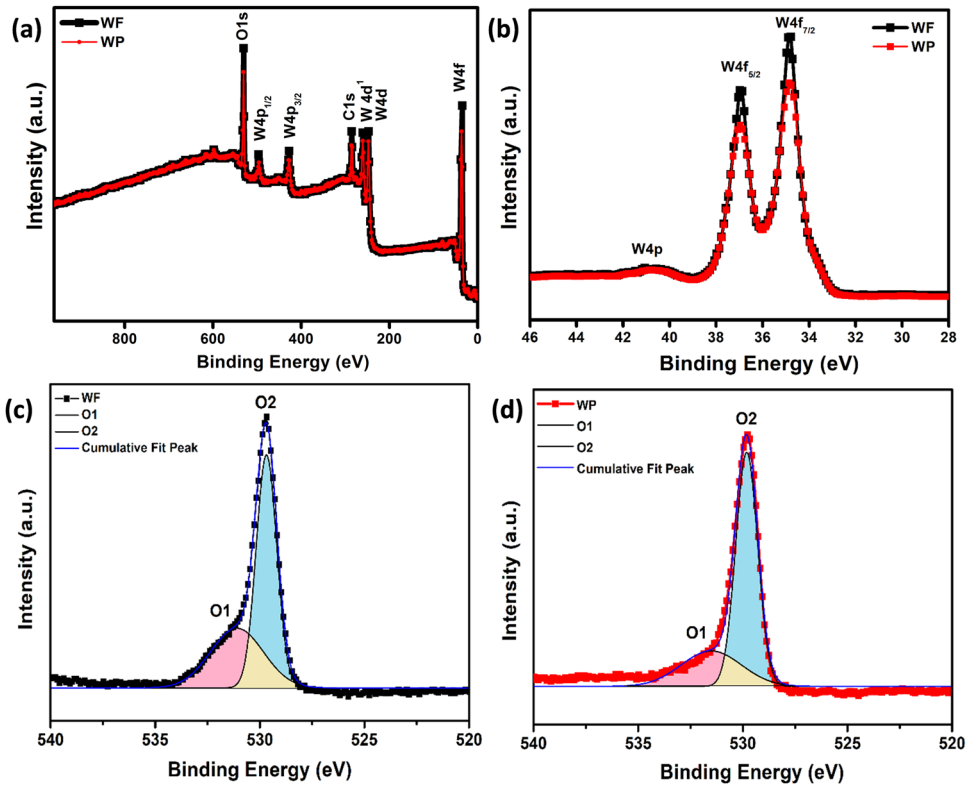

Fig. 2 (a) XPS survey spectrum, (b) XPS of spin–orbit split peaks of W 4f, and (c and d) spectral decomposition of the O 1s spectrum of WF and WP, respectively.

decreasing crystallite size. Here, due to the inter-connected orientation of nanograins in the fiber-shaped WO_3, they experienced a notable difference in the crystallite size compared to particle morphology as measured by XRD.

In order to get a more clear picture of the morphology of the fibers and particles, corresponding TEM bright-field images are depicted in Fig. 4(a), (b) and (d), (e) as obtained from the transmission electron microscopic observations. Clear disc-like structures of well separated large WO_3 grains are evident for the particles whereas the fibers are formed of well interconnected smaller grains forming a highly porous structure. The lattice structures of both the WP and WF samples are distinguished in

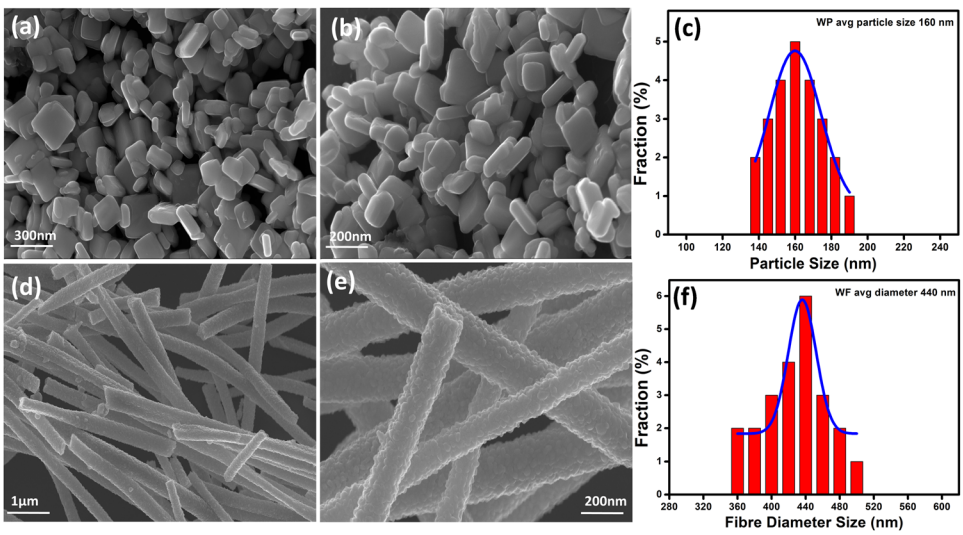

Fig. 3 FESEM microstructural images of (a) & (b) hydrothermally synthesized WO_3 nanoparticles at different magnifications, (c) corresponding histogram plot, (d) & (e) WO_3 fibers synthesized by the electrospinning technique at different magnifications, and (f) corresponding histogram plot representing the fiber diameter, respectively.

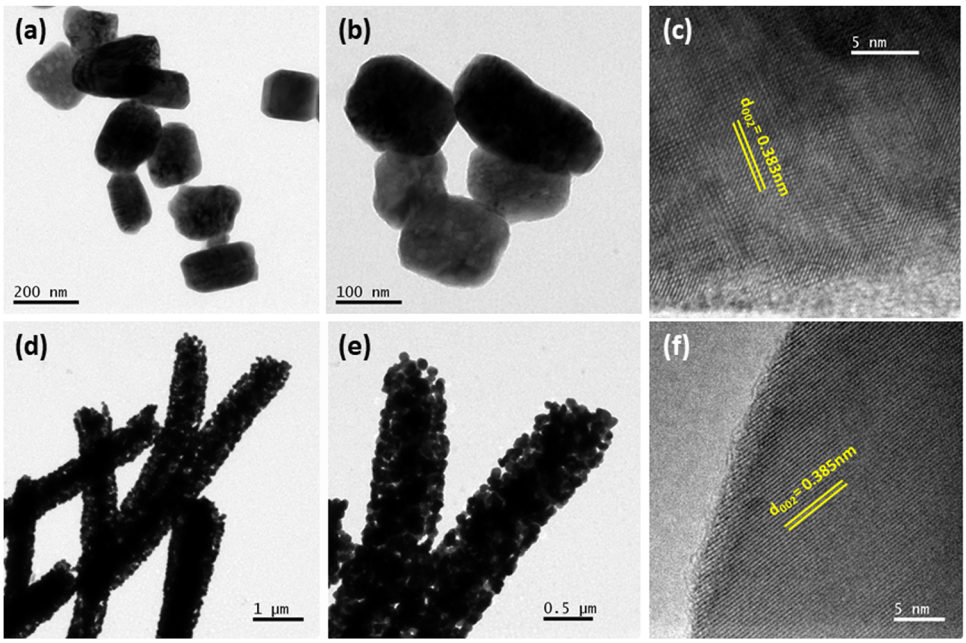

Fig. 4 (a and b) TEM bright field images of hydrothermally synthesized WO_3 nanoparticles at different magnifications, (c) corresponding HRTEM image, (d and e) TEM bright field images of WO_3 fibers synthesized by the electrospinning technique at different magnifications, and (f) corresponding HRTEM image.

the high-resolution transmission electron microscope (HRTEM) images, which are shown in Fig. 4(c) and (f), respectively. The very clear two dimensional ordered lattice structures shown in Fig. 4(c) and (f) indicate the single crystalline nature of the samples. From the HRTEM image, the interlayer spacing was calculated as 0.383 nm and 0.385 nm for the WP and WF samples, respectively, corresponding to the (002) crystal plane of the monoclinic WO_3 structure. The PVP used during synthesis is responsible for the formation of a fiber shaped 002 oriented structure The pyrrolidone group of the PVP strongly chemisorbs on the ammonium tungstate surface causing the stabilization of the (002) facet, while the aliphatic chains of the PVP stay away from the ammonium tungstate surface and act as a steric barrier, and thus help in the formation of a 1D oriented morphology. During the anisotropic growth, this difference in growth rate and capping effect will result in a step-like morphology.

BET specific surface area analysis of the synthesized WP and WF samples exhibited a surface area of $\sim$16 m^2 g^{-1} and $\sim$87 m^2 g^{-1}, respectively, as evident from the BET isotherm shown in Fig. S2(a) and (b) (ESI†), respectively. It is expected that the comparatively higher surface area of the fiber-based sample could attach more gas molecules than the particles and hence could exhibit better sensing response under identical conditions.

Gas sensing measurements

The fully characterised calcined WO_3, particles and electrospun fibers have been used as the acetone sensing material for fabricating sensor films on alumina tubes. Hereafter, the data corresponding to the particle-based sensor will be designated as WPS and that of the fibers will be designated as WFS. We measured the resistance change of both WPS and WFS sensors at different temperatures before measuring the changes in exposure to different concentrations of acetone gas. The sensing response as a function of change of resistance is measured at different operating temperatures for both WPS and WFS as shown in Fig. 5(a). Both the sensors have been exposed towards different concentrations of acetone for 15 s of exposure time, and the change of resistance was monitored. The particle-based sensor (WPS), exhibited a response of about 84% at 200 °C, and the fiber-based sensor (WFS) showed a higher sensitivity of around 90% at a comparatively lower operating temperature of 150 °C (Fig. 5(a)). In Fig. 5(b), the responses of WPS and WFS at the optimum operating temperature towards different acetone concentrations (0.5, 0.8, 1, 2, 5 and 10 ppm) are shown, which signifies the lower concentration acetone sensing ability of both the sensors under comparatively lower operating temperatures. Of late, human breath analysis has been considered as a non-invasive and rapid method for detecting various volatile organic compounds that are indicators for different diseases. Acetone in breath has been considered as a biomarker for non-invasive diagnosis of diabetes where a concentration of below 1 ppm acetone is considered as the condition in normal people. An acetone concentration in breath of above 1 ppm has been considered as the condition in patients with diabetes. From the data shown in Fig. 5(b), it is very clear that the fabricated sensors could be used for differentiating acetone in the breath of normal people and diabetic patients. Based on the highest responses exhibited, 200 °C and 150 °C have been considered as the optimum operating temperatures for the WPS and WFS sensors. As per the surface controlled mechanism of sensing, a maximum number of gas molecules are expected to react with adsorbed oxygen species at the highest operating temperature

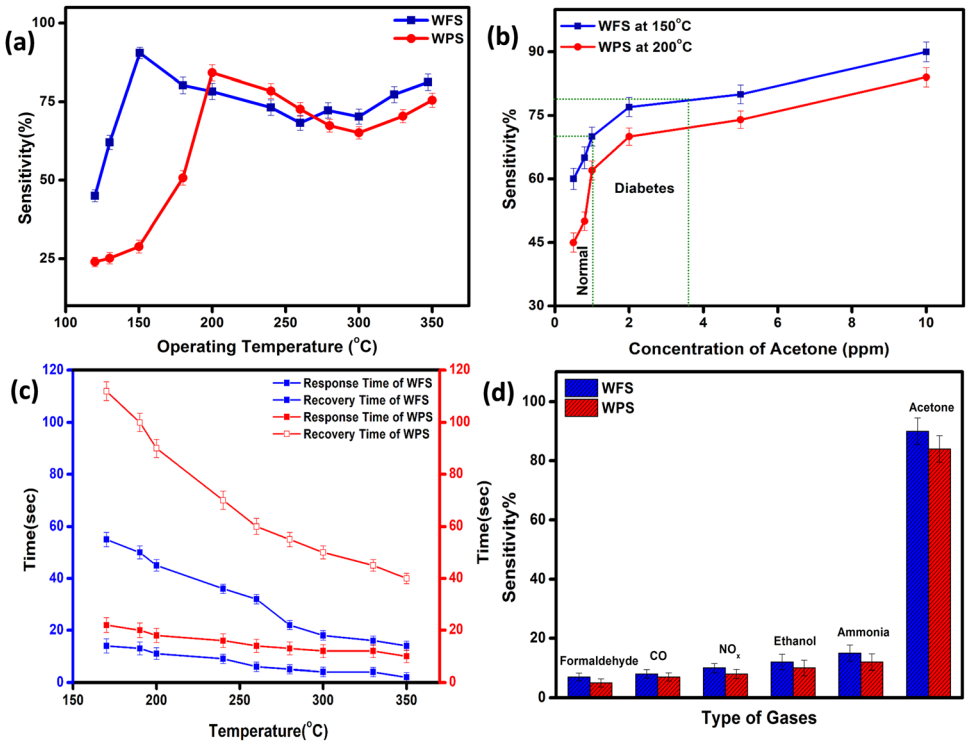

Fig. 5 (a) Variation of the sensitivity of WPS and WFS-based sensors with operating temperature at a fixed acetone concentration, (b) sensitivity plot for various concentrations of acetone (0.5, 0.8, 1, 2, 5 and 10 ppm) at the optimized operating temperature, (c) response and recovery plot as a function of different operating temperatures, and (d) cross-sensitivity plot for various gases at a similar concentration of 10 ppm for WPS and WFS, respectively.

leading to a higher resistance change.[41,42] To understand the quality of a sensor in terms of its response and recovery time on exposure to any analyte gas, the same has also been measured on exposure to 10 ppm acetone. On comparison of the response and recovery times of the two sensors (Fig. 5(c)), the very fast response and recovery of the fiber-based sensors compared to WPS is very clear. The higher surface area and the porous morphological nature of the fiber-based sensor could be one of the reasons for this improved response towards acetone.[43,44]

To examine the cross sensitivity of the fabricated sensors against different gases of the same concentration by volume and thereby determine its selectivity to any particular gas, we checked the dynamic response behavior of the fabricated sensors towards 10 ppm of different gases and the optimized results are plotted in Fig. 5(d). To analyze the cross-sensitivity, the selectivity co-efficient has been calculated by the equation: $\beta = S_{\text{acetone}}/S_{\text{gas}}$ where S_{acetone} and S_{gas} are the response of the sensor towards acetone and any other gas of 10 ppm concentration.[45] The selectivity co-efficient (β) calculated from Fig. 5(d) varied in the order $\beta_{\text{Formaldehyde}}$ (12.85) > β_{CO} (11.25) > β_{NOx} (9) > β_{Ethanol} (7.5) > β_{Ammonia} (6) for WFS and for WPS it is $\beta_{\text{Formaldehyde}}$ (16.8) > β_{CO} (14) > β_{NOx} (10.5) > β_{Ethanol} (8.4) > β_{Ammonia} (7) and from the low selectivity data it is confirmed that both the sensors have selective sensitivity towards acetone, which is highly interesting for fabricating handheld devices based on our systems for commercialization.

The dynamic response of WPS and WFS was measured on exposure to 10 ppm acetone for 15 s, as shown in Fig. 6(a) and (b). The response recovery dynamic plots of WFS and WPS at different operating temperatures are presented in Fig. S3(a)–(f) and S4(a)–(f) (ESI†). The response and recovery times calculated from the steady state dynamic curve shown in Fig. S5a and b (ESI†) were observed as 18 s and 90 s for WPS and 10 s and 40 s for WFS, respectively. The dynamic characteristics of WFS further indicate that the sensors respond faster with high sensing capability compared to WPS. The sensors' sensitivity can be explained by the Freundlich adsorption isotherm equation[46] as given in eqn (iii). To further understand the high sensitivity of WFS, various absorption isotherm models were studied, which signifies the interaction between the sensor material surface and target gas molecules.

$$S \propto aC^b/(1 + aC^b) \quad \text{(iii)}$$

where C represents acetone concentration, a is the proportionality factor, and b is the exponent.[47] In our work, the concentration of acetone is low (< 1 ppm), and hence $aC^b \rightarrow 0$, so eqn (iii) is thus modified as,

$$S \propto aC^b \quad \text{(iv)}$$

The above eqn (iv) can be converted to:

$$\log S = \log a + b \log C \quad \text{(v)}$$

The power law relation between the responses of the particle (WPS) and fiber (WFS)-based sensors and the acetone concentration is presented in Fig. 6(c). The value of b calculated from the slope of the $\log S$ *vs.* $\log C$ plot is lower than 1, and the

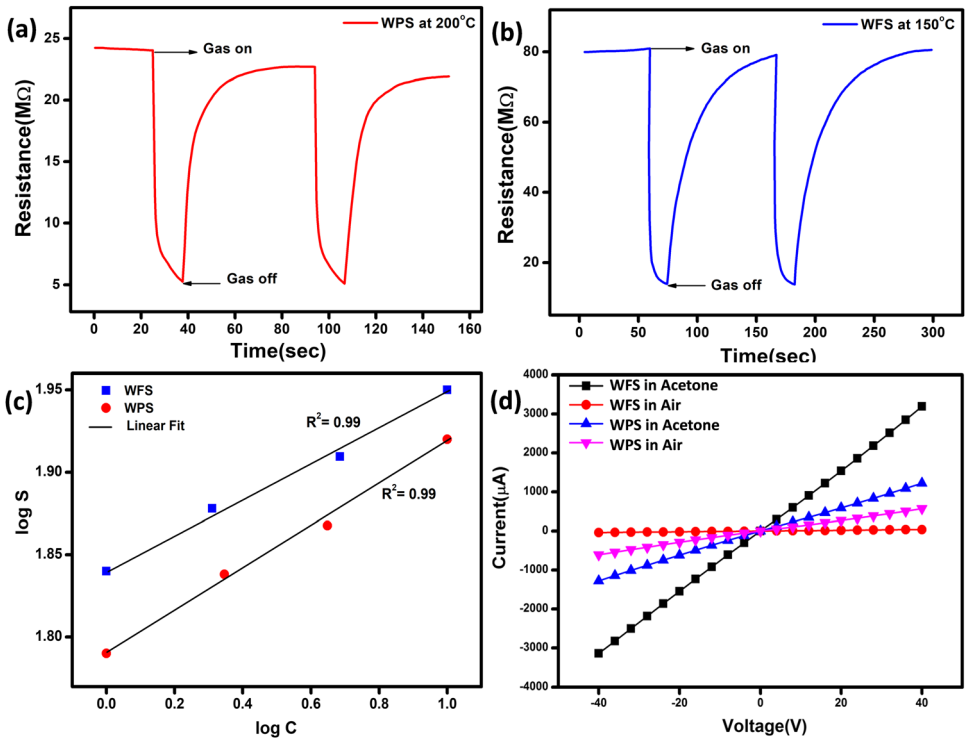

Fig. 6 Dynamic response curve of (a) WPS and (b) WFS, (c) log *C* *vs.* log *S* plot and (d) *I*–*V* diagram for the WPS and WFS sample in the presence of acetone and air.

experimental data's linear fitting shows the sensor's ability to detect a lower concentration range of acetone, which is more desirable for sensing applications. Fig. 6(d) shows *I*–*V* characteristics measured at −40 V to +40 V bias voltage ranges at an operating temperature of 150 °C for WFS and 200 °C for WPS, respectively, in air and 10 ppm acetone indicating a linear ohmic response for both particle and fiber-based sensors. The ohmic behaviour of the *I*–*V* plot of the fabricated sensors is an ideal situation to achieve an optimized response from a semiconductor device.

The sensing response of the devices could be influenced by the relative % humidity (RH) of the measurement environment. Referring to the reported literature,[48,49] we have prepared a relatively humid environment with saturated solutions of inorganic salts in a closed chamber (Table S1, ESI†). Both the sensors were exposed to this solution for a continuous duration of 6 h and the sensing performance was monitored in the presence of 10 ppm acetone. It is noticeable from Fig. S6 (ESI†) that the performance of both the sensors at 10 ppm exhibited a slight variation with increase in relative humidity (% RH).

To further demonstrate the potential of the WFS sensor in fabricating sensors for breath analysis, we have monitored the performance of the WFS sensor in two different concentrations of acetone, namely 10 ppm and 1 ppm at various relative humidities (RH) as shown in Fig. 7. It is noticeable that the performance of the sensor exhibited only a slight decrease in performance with the increase in relative humidity (% RH) under both conditions.

Based on the results, it can be inferred that the response of the sensor towards both higher and lower concentrations of acetone is high, thereby establishing the potential of the sensor for the detection of acetone in breath having high RH content.

In addition, we have also measured the performance of WFS as a function of various concentrations of acetone at different RH conditions as shown in Fig. 8. In all the cases there is a distinct difference in the response of the sensor at high ppm acetone concentration and low ppm acetone concentration at all RH conditions investigated. This data further confirms the potential of the developed material in fabricating an acetone sensitive and selective sensor for the analysis of breath for diseases like diabetes.

In addition, we have also checked the performance of the WFS sensor in the presence of various other interfering gases under 84% relative humidity as demonstrated in Fig. S7 (ESI†).

In order to monitor the stability, the responsive nature of both the sensors was monitored under ambient conditions for more than three months, and high stability was exhibited by the particle and fiber-based sensors as there was no observable change in resistance within the studied period, which is shown in Fig. 9(a) and (b), and the calculated sensitivity stability for both sensors is shown in Fig. 9(c). Such impressive stability is favourable for making devices as the material used appears stable in the ambient conditions.

In addition to the DC measurements discussed above, AC electrical measurements were also performed to correlate the response parameters in the presence of acetone within the frequency range of 100 Hz to 1 MHz. From impedance spectroscopy studies, it is easy to interpret the contribution from the bulk, inter grain and electrode towards the response of a sensor device. As we

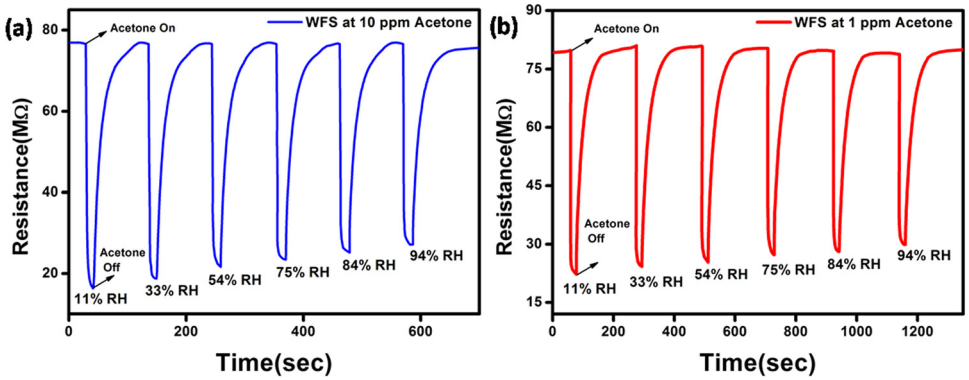

Fig. 7 Dynamic response curve of the WFS sensor as a function of different % RH towards (a) 10 ppm and (b) 1 ppm of acetone.

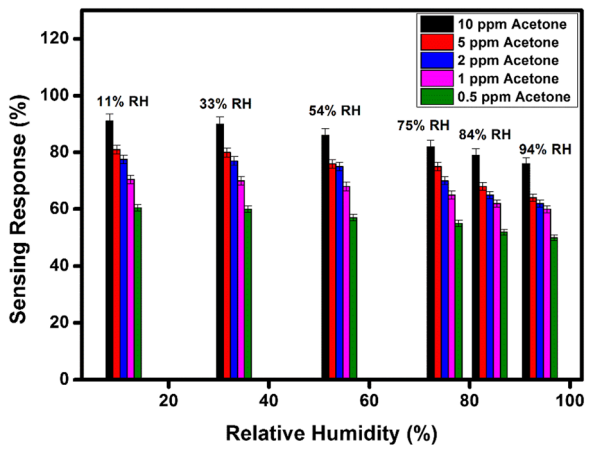

Fig. 8 Sensitivity response bar diagram of the WFS sample as a function of different % RH towards different concentrations of acetone (10, 5, 2, 1 and 0.5 ppm).

are trying to understand the sensing mechanism, the impedance characteristics were determined to clearly understand the contribution of the intra-grain, grain boundary and electrode interfaces in the material.

The impedance plot is one of the significant techniques to calculate the electrical parameters of the active region of a sensor material by plotting Z'' (the reactive imaginary part) against Z' (the real resistive part). The Nyquist diagram in Fig. 10(a) and (b) represents an explicit semi-circle nature of WPS and WFS in the presence of acetone at different operating temperatures from 100 °C to 350 °C. In the case of a defect-free homogeneous sensor material, an apparent semi-circle will be evident in the Nyquist plot, with its origin lying exactly on the real axis.[50] The bulk grain contribution, including surface and grains, appears as a first semi-circle, whereas the grain boundary and electrode interface contribution appear as subsequent semi-circles.[51] In our case, only a single semi-circle was seen in the impedance graph measured in air. Since this semi-circle is mainly due to the bulk contribution, the influence of grain boundaries is expected to be negligible in the acetone detection process of the studied samples. In addition, the impedance of both sensors decreases when exposed to acetone.

By using the *Z*-View2 software, the Z' and Z'' calculation from the impedance data has been analyzed in a wide range of frequency (100 Hz–1 MHz) and temperature (100–350 °C) for both the particle and fiber-based sensors in the presence of 10 ppm concentration acetone as shown in Fig. 10(a) and (b). The Arrhenius equation can show the relationship between grain resistance and temperature:

$$R = R_o \exp\left(E_a/KT\right) \quad \text{(vi)}$$

Here, E_a is the activation energy, K is Boltzmann's constant, T is the temperature in Kelvin (K), and R_o can be described as a pre-exponential factor. The activation energy has been calculated from the slope of the ln (R) *vs.* $1/KT$ graph, as shown in Fig. 10(c) and (d) for WPS and WFS, respectively. The linear absorption behaviour suggests a single rate-limiting step that could govern the acetone sensing behaviour within this temperature region. The calculated activation energy is 0.356 eV and 0.226 eV for WPS and WFS, respectively, and is also enlisted in Table 1. The calculated high activation energy confirms chemisorption as the rate-limiting activation process responsible for the acetone detection mechanism in both cases.

A parallel resistance–capacitance (RC) circuit models the impedance data for the particle and fiber-based sensors. The RC parameters have been calculated from the RC model circuit. The Nyquist diagram of WPS and WFS in the presence of air and 10 ppm of acetone has been plotted in Fig. 11(a) and (b), respectively. It is noticed that the data can be fitted with only one symmetric semi-circle in the case of the WPS and an asymmetric semi-circle for the WFS, which is probably due to a mild overlap of the grains and grain boundaries possibly originating from nanocrystalline features of the fibers as evident from the microstructural studies shown in Fig. 4. For the fiber-based sample, as there is an indication of an overlapped second semi-circle in the main semi-circle, indicating weak evidence of the grain boundaries' influence on the sensing response.[52–54] The equivalent circuit, along with the Nyquist diagram of WPS and WFS in the presence of 10 ppm acetone, is presented as an inset in Fig. 11(c) and (d), respectively.

It can be optimized that the impedance decreases after exposure to acetone at constant operating temperature, and the sensitivity (S) of the sensor can also be calculated from the

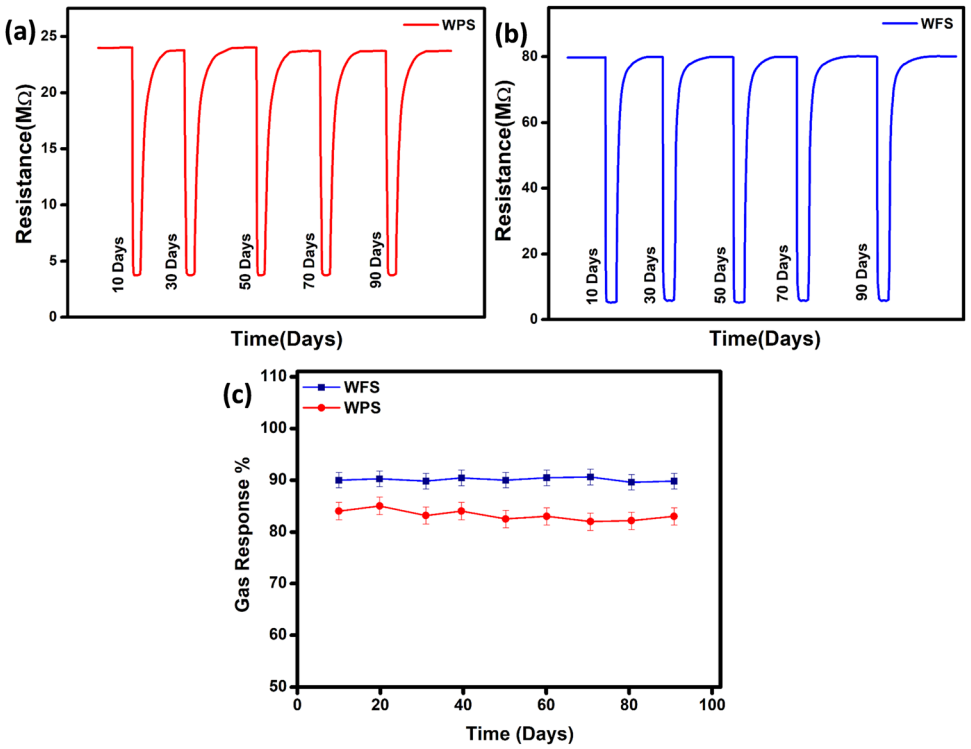

Fig. 9 Stability in change of resistance of (a) hydrothermally synthesized particle and (b) electrospun fiber-based sensors with time and (c) sensitivity stability of both sensors.

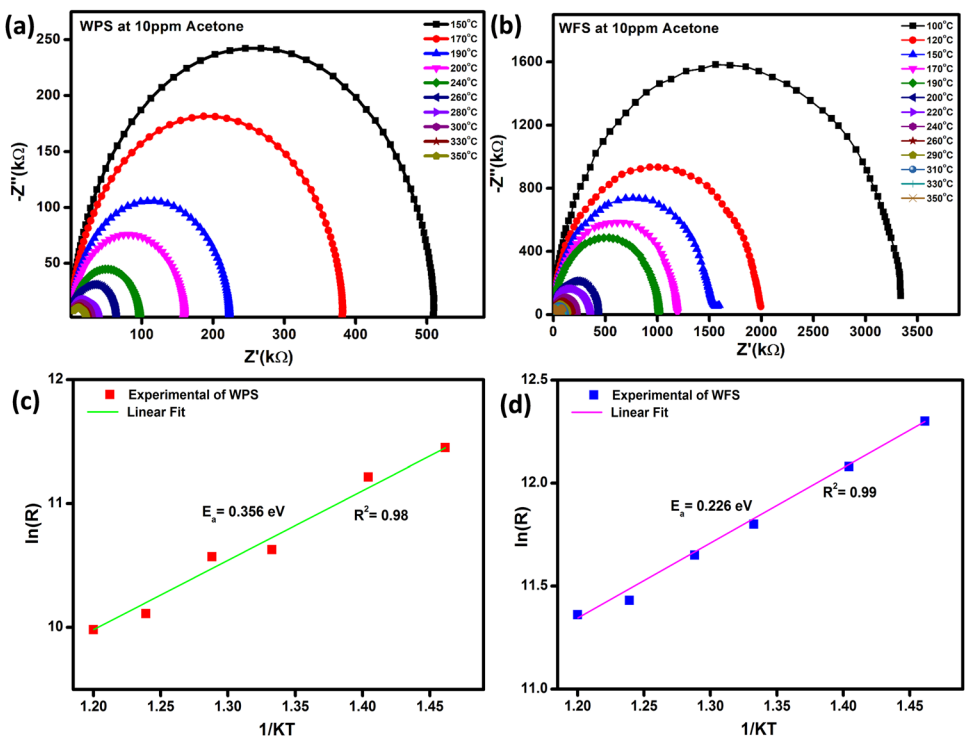

Fig. 10 (a and b) Nyquist plot at different operating temperatures, and (c and d) corresponding calculated activation energy of WPS and WFS, respectively.

Table 1 Comparison of sensitivity response calculated from AC and DC methods

Sensor material	Surface area (m^2 g^{-1})	Activation energy (eV)	Sensitivity from AC impedance (%)	Sensitivity from DC resistance (%)
Particle	15.48	0.36	82.5	84
fiber	85.65	0.23	93.1	90

impedance data (Z'') as $S(\%) = \frac{Z''_{Air} - Z''_{Acetone}}{Z''_{Air}}$. The Nyquist plots correspond to the maximum impedance imaginary part in the presence of acetone and air under relaxation frequency. The sensitivity was calculated from the data, ~82.5% and ~93.1%, respectively, for WPS and WFS, which is quite similar to the results obtained from the DC measurements shown in Table 1.

Gas sensing mechanism

The gas sensing mechanism and sensing response of a semiconductor metal oxide-based gas sensor mainly depend on the resistance variation due to the adsorption–desorption phenomenon occurring on the sensor surface. The variation of surface resistance with temperature for both the sensors is shown in Fig. 12. The sensor's surface resistance decreases with the increase of the operating temperature, in the range of 100–120 °C for fibers and 130–160 °C for particles, which is mainly due to the physisorption of the oxygen molecules in air. With increased temperature, the electrons from the conduction band of the material get trapped on the surface, resulting in ionization of the physisorbed oxygen molecules into adsorbed oxygen species like O^{2-}, O_2^- and/or O^-. During this process, the concentration of electrons on the material's surface decreases due to various reactions, resulting in an electron depletion layer followed by an increase in the sensor's resistance in air, as shown in Fig. 12.

The gas sensing mechanism of a typical resistive SMO-based device involves two essential functions, *viz.* (i) recognition of a target gas through gas–solid interaction, which induces an electronic change of the oxide surface, *i.e.* receptor function, and (ii) transduction of the surface phenomenon into a resulting change in ionosorbed (physisorbed and chemisorbed both are possible) oxygen is reflected as a change in electrical resistance of the sensor material, *i.e.* transducer function. Chemisorbed acetone then undergoes a chemical reaction with the lattice oxygen, accompanied by a significant conductivity enhancement.[55] When the WO_3-based sensor is exposed to the analyte gas acetone, which is a reducing gas, the target gas molecules react with adsorbed oxygen species (O^- and O^{2-}) which are produced on the surface of the sensor material and release the free electrons back to the conduction band of the WO_3 leading to a further decrease in the electron depletion layer. As a result, the electrical resistance of the material also decreases. The overall sensing mechanism has been described as shown in the following equations by many investigators,[56–58]

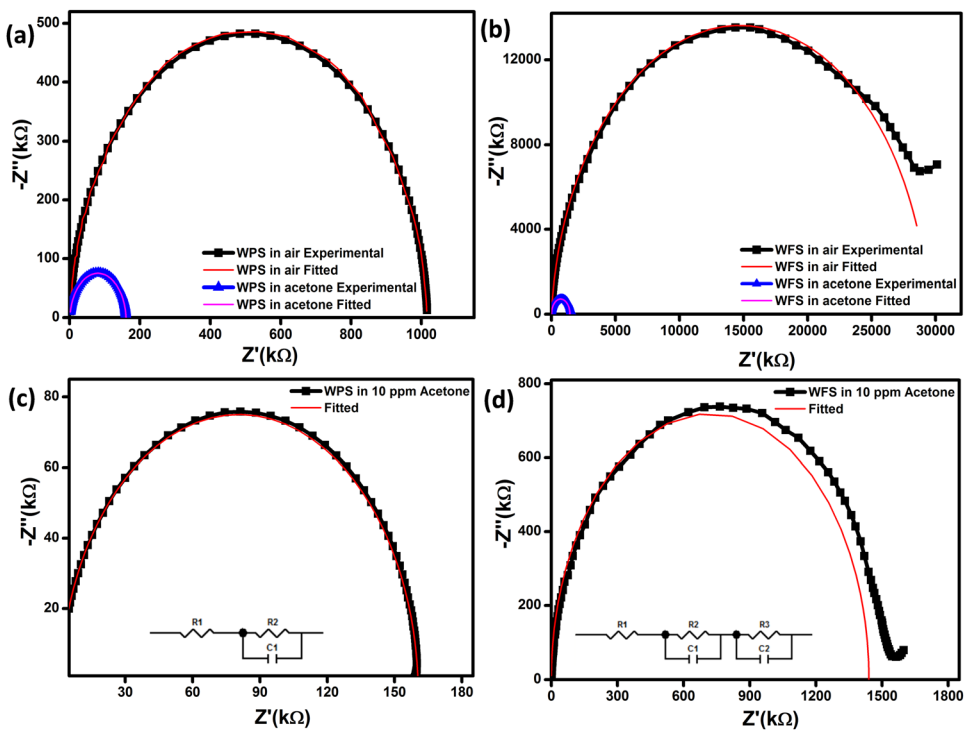

Fig. 11 Nyquist plots of (a) WPS and (b) WFS in the presence of air and 10 ppm acetone, respectively, and enlarged version of the Nyquist plots for (c) WPS, and (d) WFS in 10 ppm acetone, respectively (inset: corresponding equivalent circuit diagram).

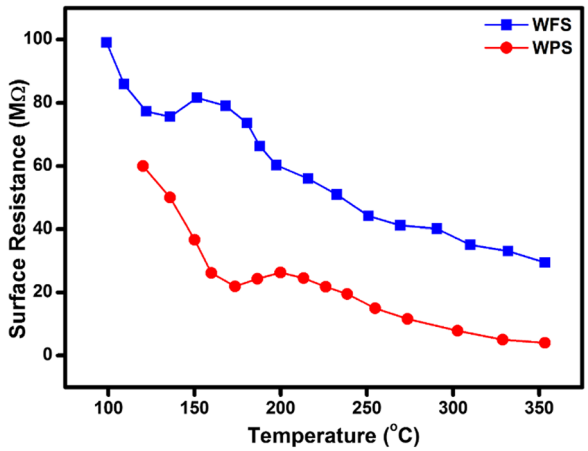

Fig. 12 Comparative surface resistance variation plot as a function of temperature in the presence of air for WFS and WPS.

$$(O_2)_{gas} \leftrightarrow (O_2)_{ads} \quad \text{(vii)}$$

$$(O_2)_{ads} + e^- \leftrightarrow {O_2}^-_{ads} \quad \text{(viii)}$$

$$CH_3COCH_3 + 4{O_2}^-_{ads} \rightarrow 3CO_2 + 3H_2O + 4e^- \quad \text{(ix)}$$

The ionosorbed species act as electron acceptors due to their relative energetic position concerning the Fermi level and electron affinity. The reaction of these oxygen species with reducing gases or a competitive adsorption–desorption or replacement of the metastable adsorbed oxygen species by other molecules decreases and can reverse the band bending in the opposite direction with improved conductivity and less band bending. The surface ionosorbed O_2^- was reported to form at 300–450 °C for most SMO sensors.[59] In this work, the WO_3-fibers can operate at a much lower temperature, 150 °C, to meet this surface ionosorbed process. At higher operating temperatures, excessive temperature increases may lead to a considerable drop in gas response due to the simultaneous desorption of adsorbed oxygen from the exposed surface of the sensors. Secondly, with increased operating temperature, a gas response will be predominantly determined by the change of bulk properties and not by the surface properties of the materials. Hence, the synthesized fibers can eliminate all the above mentioned complications to accelerate the sensing mechanism with rapid response and longer cycles. Besides, an advantage of the porous 1D nanostructure is that it can facilitate O_2^- ionosorption. In addition, the fiber morphology can benefit from the highly conductive 1D nanostructure and the increased surface area and porosity available for faster

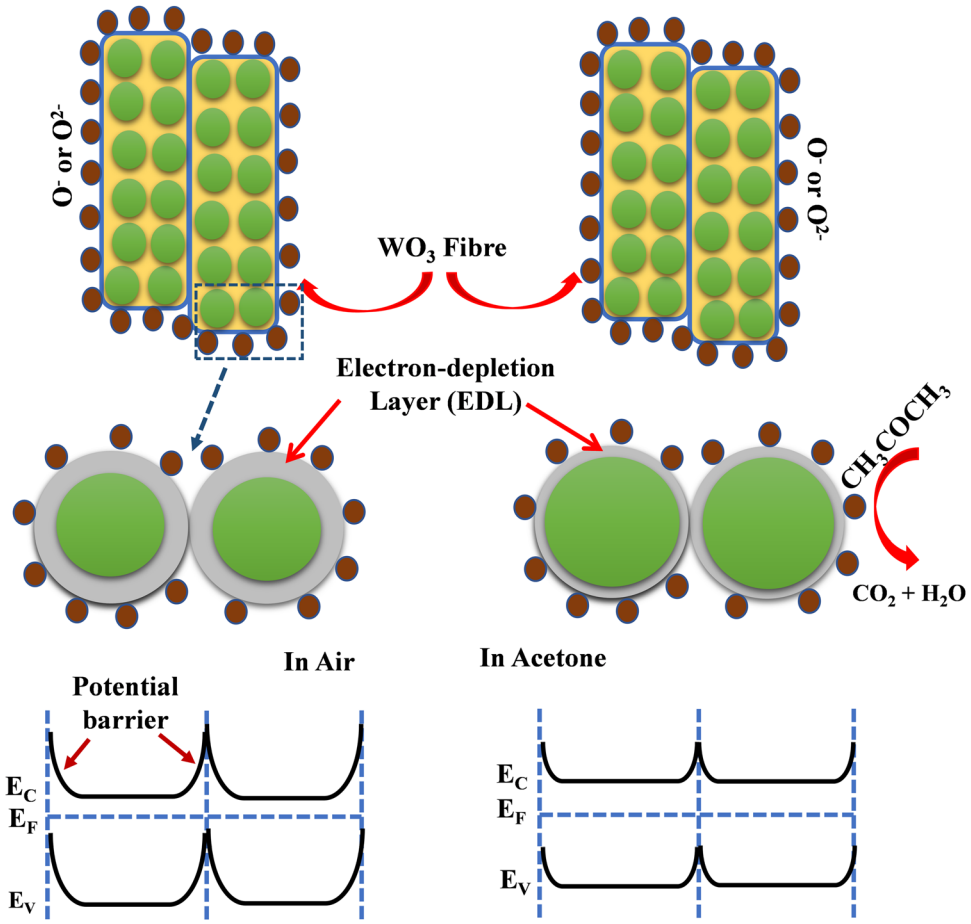

Scheme 1 Acetone sensing mechanism of the fabricated fiber-based sensor.

Table 2 A comparison of the response of the sensors

Sensor material	Operating temperature (°C)	Sensitivity	Response time (s)	Recovery time (s)	Detection acetone conc (ppm)	Selectivity	Ref.
WO_3 composite with graphene	300	6.7	7	18	5	Ethanol ammonia (100 ppm)	18
WO_3 hollow-sphere	400	3.53	—	—	50	H_2S, NH_3 alcohol, CS_2 (50 ppm)	63
Nanofiber	350	1.79	33	44	12.5	CO_2 (500 ppm)	64
Apoferritin-PtY loaded nanofiber	350	50	20	33	1	H_2, H_2S, $C_6H_5CH_3$, CO, ethanol, NH_3, pentane, CH_4, and methyl mercaptan (1 ppm)	66
La_2O_3–WO_3 nanofibers composite	350	12.7	6	210	100	Ethanol, methanol, methanol, benzene, toluene and ammonia (100 ppm)	65
3 mol% Cu doped hollow nanofiber	300	6.43	5	20	20	Carbon dioxide, ethylene glycol, methanol and ammonia, isopropyl alcohol, methanol, toluene, ethanol, *n*-butanol (20 ppm)	67
Pt loaded porous fiber	400	28.9			5	CO, ethanol, NH_3, toluene, H_2S (5 ppm)	62
Fe doped rGO decorated WO_3	130	4.6	20	75	10	Ethanol, ammonia, formaldehyde, carbon monoxide and methane (10 ppm)	68
10% Si doped composite with WO_3	300	4.6	1.3 min	1.4 min	0.6	Ethanol (600 ppb)	19
WO_3 fiber	**150**	**90** **60**	**10**	**40**	**10** **0.5**	Formaldehyde, CO, NOx, ethanol, ammonia (1 ppm)	**This Work**

sensing performance compared to particles as shown in Scheme 1.

We compared the performance of our best-performing fiber material with what is available in the literature on WO_3 fiber-based sensors reported in the literature towards <50 ppm acetone, as shown in Table 2. In most of the reported cases, both the concentration and operating temperatures are high compared to the performance of the sensors presented in the present work. It is also surprising to find that we could not find the response in the presence of moisture for any of the reported cases of WO_3-based sensors.

It has also been reported that the (002) facets are the most active planes with superior reactivity in nanoparticulate form.[60,61] Therefore, based on the reported data, it could be confirmed that the preferential orientation of (002) planes of WO_3 could be more favourable in the adsorption–desorption of gas molecules leading to an enhanced response towards acetone at a lower temperature. Based on our data, the factors responsible for the improved acetone sensing characteristics of the WO_3 fibers can be summarized as (i) the presence of an enhanced 002 facetted structure because (002) facets with an asymmetric distribution of O atoms induce a large number of dipole moments, which can help in the adsorption and reaction between the (002) facets and acetone molecules, (ii) high surface area and porosity leading to better adsorption and desorption of oxygen at a lower temperature, and (iii) lower activation energy as calculated from impedance measurements.

Conclusion

In conclusion, γ-monoclinic WO_3 fibers with highly reactive exposed (002) facets have been synthesized by the electrospinning technique for fabricating tubular sensors for acetone detection. A comparative study between WO_3 particles and fibers has been undertaken to understand the various factors, including the shape of the oxide particles, on acetone sensing. We also compared the response of the sensors using both AC and DC measurements which are complimentary techniques in understanding the sensing mechanism. Through various characterization techniques, it has been demonstrated that by modifying the crystal facets of WO_3 it is possible to fabricate sensors exhibiting preferred response towards different concentrations of acetone, which will be useful for developing acetone sensors for the diagnosis of acetone from breath. Based on various studies it has been confirmed that the morphological changes did not have any dramatic effect on the sensing properties. Moreover, AC measurements and modeling confirm that it is mainly the grains and the grain surfaces that are involved in the detection of acetone in both cases. The fabricated WFS sensor demonstrated an excellent $\sim$90% sensing response in the presence of 10 ppm acetone at a low temperature ($\sim$150 °C) with a fast response ($\sim$10 s) and recovery ($\sim$40 s) time. To conclude, an outstanding response to both low and high ppm acetone gas in high relative humidity conditions with improved selectivity and stability projects WO_3 fibers as a promising material to fabricate acetone sensors for non-invasive diagnosis of diabetes in breath.

Conflicts of interest

We declare that there is no conflict of interest.

Acknowledgements

PG gratefully acknowledges the INSPIRE program of the Department of Science and Technology (DST), Govt. of India, for the PhD fellowship. M. Manikandan acknowledges University Grant Commission for the Junior Research Fellowship. The authors acknowledge the help of Mousumi Narjinary, Senior Technical Officer, Material Characterization & Instrumentation

Division, CSIR-Central Glass and Ceramic Research Institute (CGCRI), Jadavpur, Kolkata 700032, for initial help in the sensing measurements. The authors also thank the Director, CGCRI and the Director, National Institute for Interdisciplinary Science and Technology, for all the support extended during the execution of the work.

References

1 Y. Broza and H. Haick, *Nanomedicine*, 2013, **8**, 785–806.
2 C. Dong, R. Zhao, L. Yao, Y. Ran, X. Zhang and Y. Wang, *J. Alloys Compd.*, 2020, **820**, 153194.
3 A. I. Khudadad, A. A. Yousif and H. R. Abed, *Mater. Chem. Phys.*, 2021, **269**, 124731.
4 X. Chang, S. Xu, S. Liu, N. Wang, S. Sun, X. Zhu, J. Li, O. Ola and Y. Zhu, *Sens. Actuators, B*, 2021, **343**, 130135.
5 H. Xu, J. Gao, M. Li, Y. Zhao, M. Zhang, T. Zhao, L. Wang, W. Jiang, G. Zhu, X. Qian, Y. Fan, J. Yang and W. Luo, *Front. Chem.*, 2019, **7**, 266.
6 R. Jiang, B. Li, C. Fang and J. Wang, *Adv. Mater.*, 2014, **26**, 5274–5309.
7 M. Righettoni, A. Amann and S. E. Pratsinis, *Mater. Today*, 2015, **18**, 163–171.
8 L. Zhou, J. Zou, M. Yu, P. Lu, J. Wei, Y. Qian, Y. Wang and C. Yu, *Cryst. Growth Des.*, 2008, **8**, 3993–3998.
9 J. Li, J. W. Zhu and X. H. Liu, *New J. Chem.*, 2013, **37**, 4241–4249.
10 Z. X. Cai, H. Y. Li, X. N. Yang and X. Guo, *Sens. Actuators, B*, 2015, **219**, 346–353.
11 G. Wang, Y. Ji, X. R. Huang, X. Q. Yang, P. R. Gouma and M. Dudley, *J. Phys. Chem. B*, 2016, **110**, 23777–23782.
12 T. A. Nguyen, S. Park, J. B. Kim, T. K. Kim, G. H. Seong, J. Choo and Y. S. Kim, *Sens. Actuators, B*, 2011, **160**, 549–554.
13 S. H. Wei, G. Y. Zhao, W. M. Du and Q. W. Tian, *Vacuum*, 2016, **124**, 32–39.
14 X. Han, X. Han, L. Lia and C. Wang, *New J. Chem.*, 2012, **36**, 2205–2208.
15 A. Staerz, U. Weimar and N. Barsan, *Sensor*, 2016, **16**, 1815.
16 N. Zhang, S. Ruan, Y. Yin, S. Wen and Y. Chen, *ACS Appl. Nano Mater.*, 2018, **1**, 4671.
17 C. Deng, J. Zhang, X. Yu, W. Zhang and X. Zhang, *J. Chromatogr. B: Anal. Technol. Biomed. Life Sci.*, 2004, **810**, 269–275.
18 S. Sun, X. Xiong, J. Han, X. Chang, N. Wang, M. Wang and Y. Zhu, *ACS Appl. Nano Mater.*, 2019, **2**, 1313–1324.
19 M. Righettoni, A. Tricoli and S. E. Pratsinis, *Anal. Chem.*, 2010, **82**, 3581–3587.
20 Y. Zhang, W. He, H. Zhao and P. Li, *Vacuum*, 2013, **95**, 30–34.
21 L. Wang, A. Teleki, S. E. Pratsinis and P. I. Gouma, *Chem. Mater.*, 2008, **20**, 4794–4796.
22 O. O. Abe, Z. Qiu, J. R. Jinschek and P. I. Gouma, *Sensors*, 2021, **21**, 1690.
23 S. J. Choi, S. Chattopadhyay, J. J. Kim, S. J. Kim, H. L. Tuller, G. C. Rutledge and I. D. Kim, *Nanoscale*, 2016, **8**, 9159–9166.
24 J. Y. Leng, X. J. Xu, N. Lv, H. T. Fan and T. Zhang, *J. Colloid Interface Sci.*, 2011, **356**, 54–57.
25 M. Yin, L. Yu and S. Liu, *J. Alloys Compd.*, 2017, **696**, 490–497.
26 A. Labidi, C. Jacolin, M. Bendahan, A. Abdelghani and J. Guerin, *Sens. Actuators, B*, 2005, **106**, 713–718.
27 Q. Q. Jia, H. M. Ji, D. H. Wang, X. Bai, X. H. Sun and Z. G. Jin, *J. Mater. Chem. A*, 2014, **2**, 13602–13611.
28 J. J. Qi, S. Gao, K. Chen, J. Yang, H. W. Zhao, L. Guo and S. H. Yang, *J. Mater. Chem. A*, 2015, **3**, 18019–18026.
29 J. Zhang, P. Zhang, T. Wang and J. Gong, *Nano Energy*, 2015, **11**, 189–195.
30 I. Vamvasakis, I. Georgaki, D. Vernardou, G. Kenanakis and N. Katsarakis, *J. Sol-Gel Sci. Technol.*, 2015, **76**, 120–128.
31 S. Wei, G. Zhao, W. Du and Q. Tian, *Vacuum*, 2016, **124**, 32–39.
32 P. Nag, S. Banerjee, Y. Lee, A. Bumajdad, Y. Lee and P. S. Devi, *Inorg. Chem.*, 2012, **51**, 844–850.
33 P. Ghosh, A. Roy, S. Mukhopadhyay, M. Narjinary, S. Sundaram, S. Sen and P. S. Devi, *Adv. Electron. Mater.*, 2021, 2000785.
34 H. Parangusan, D. Ponnamma and M. A. A. Al-Maadeed, *Sci. Rep.*, 2018, **8**, 754.
35 S. Wei, S. Li, R. Wei, S. Liu and W. Du, *Sens. Actuators, B*, 2020, **329**, 129188.
36 Q. Jia, H. Ji, D. Wang, X. Bai, X. Sun and Z. Jin, *J. Mater. Chem. A*, 2014, **2**, 13602.
37 R. F. Garcia-Sanchez, T. Ahmido, D. Casimir, S. Baliga and P. Misra, *J. Phys. Chem. A*, 2013, **117**, 13825.
38 M. Arai, S. Hayashi, K. Yamamoto and S. S. Kim, *Solid State Commun.*, 1990, **75**, 613–616.
39 S. Ramkumar and G. Rajarajan, *Appl. Phys. A: Mater. Sci. Process.*, 2017, **123**, 401.
40 R. Ji, D. Zheng, C. Zhou, J. Cheng, J. Yu and L. Li, *Materials*, 2017, **10**, 820.
41 Q. Q. Jia, H. M. Ji, D. H. Wang, X. Bai, X. H. Sun and Z. G. Jin, *J. Mater. Chem. A*, 2014, **2**, 13602–13611.
42 S. Amrehn, X. Wu and T. Wagner, *ACS Sens.*, 2018, **3**, 191–199.
43 X. M. Xu, P. L. Zhao, D. W. Wang, P. Sun, L. You and Y. F. Sun, *Sens. Actuators, B*, 2013, **176**, 405–412.
44 J. R. Huang, Y. J. Dai, C. P. Gu, Y. F. Sun and J. H. Liu, *J. Alloys Compd.*, 2013, **575**, 115–122.
45 S. Banerjee, A. Bumajdad and P. S. Devi, *Nanotechnology*, 2011, **22**, 275506.
46 J. L. Johnson, A. Behnam, Y. An, S. J. Pearton and A. Ural, *J. Appl. Phys.*, 2011, **109**, 124301.
47 Y. Dan, Y. Lu, N. J. Kybert, Z. Luo and A. T. C. Johnson, *Nano Lett.*, 2009, **9**, 1472–1475.
48 G. Jeevitha, R. Abhinayaa, D. Mangalaraj, N. Ponpandian, P. Meena, V. Mounasamy and S. Madanagurusamy, *Nanoscale Adv.*, 2019, **1**, 1799–1811.
49 L. Chen, L. Huang, Y. Lin, L. Sai, Q. Chang, W. Shi and Q. Chen, *Sens. Actuators, B*, 2018, **255**, 1482–1490.
50 Z. Ling, C. Leach and R. Freer, *Sens. Actuators, B*, 2002, **87**, 215–221.
51 K. Aguir, A. Labidi and C. L. Mauriat, *IEEE Sens.*, 2006, 267–270.

52 X. Wang, S. S. Yee and W. P. Carey, *Sens. Actuators, B*, 1995, **25**, 454–457.
53 J. Tamaki, Z. Zhang, K. Fujimori, M. Akiyama, T. Harada, N. Miura and N. Yamazoe, *J. Electrochem. Soc.*, 1994, **141**, 2207.
54 A. Labidi, C. Lambert-Mauriat, C. Jacolin, M. Bendahan, M. Maaref and K. Aguir, *Sens. Actuators, B*, 2006, **119**, 374–379.
55 P. V. Shinde, A. Patra and C. S. Rout, *J. Mater. Chem. C*, 2022, **10**, 10196.
56 S. Americo, E. Pargoletti, R. Soave, F. Cargnoni, M. I. Trioni, G. L. Chiarello, G. Cerrato and G. Cappelletti, *Electrochim. Acta*, 2021, **371**, 137611.
57 Y. Chen, H. Qin, Y. Cao, H. Zhang and J. Hu, *Sensors*, 2018, **18**, 3425.
58 P. Nag, S. Majumdar, A. Bumajdad and P. S. Devi, *RSC Adv.*, 2014, **4**, 18512.
59 K. Yuan, C. Y. Wang, L. Y. Zhu, Q. Cao, J. H. Yang, X. X. Li, W. Huang, Y. Y. Wang, H. L. Lu and D. W. Zhang, *ACS Appl. Mater. Interfaces*, 2020, **12**, 14095–14104.
60 Y. Guo, X. Quan, N. Lu, H. Zhao and S. Chen, *Environ. Sci. Technol.*, 2007, **41**, 4422–4427.
61 J. Zhang, P. Zhang, T. Wang and J. Gong, *Nano Energy*, 2015, **11**, 189–195.
62 S. J. Choi, S. J. Kim, H. J. Cho, J. S. Jang, Y. M. Lin, H. L. Tuller, G. C. Rutledge and I. D. Kim, *Small*, 2016, **12**, 911–920.
63 X. L. Li, T. J. Lou, X. M. Sun and Y. D. Li, *Inorg. Chem.*, 2004, **43**, 5442–5449.
64 M. Imran, S. S. A. A. H. Rashid, Y. Sabri, N. Motta, T. Tesfamichael, P. Sonar and M. Shafiei, *J. Mater. Chem. C*, 2019, **7**, 2961–2970.
65 C. Feng, C. Wang, P. Cheng, X. Li, B. Wang, Y. Guan, J. Ma, H. Zhang, Y. Sun, P. Sun, J. Zheng and G. Lu, *Sens. Actuators, B*, 2015, **221**, 434–442.
66 S.-J. Kim, S.-J. Choi, J.-S. Jang, N.-H. Kim, M. Hakim, H. L. Tuller and I.-D. Kim, *ACS Nano*, 2016, **10**, 5891–5899.
67 X. Bai, H. Ji, P. Gao, Y. Zhang and X. Sun, *Sens. Actuators, B*, 2014, **193**, 100–106.
68 S. Sen, S. Maity and S. Kundu, *Sens. Actuators, B*, 2022, **361**, 131706.